Scientific Reports

https://doi.org/10.1038/s41598-026-43670-x

Article in Press

Optimizing robot weaving width improves the microstructure and mechanical performance of 4043 aluminum alloy in CMT-WAAM

Received: 6 February 2026

Accepted: 5 March 2026

Published online: 18 March 2026

Cite this article as: Liu S., Sun Y., Yuan X. *et al.* Optimizing robot weaving width improves the microstructure and mechanical performance of 4043 aluminum alloy in CMT-WAAM. *Sci Rep* (2026). https://doi.org/10.1038/s41598-026-43670-x

Shuangyao Liu, Yipu Sun, Xi Yuan, Haozhong Lv, Ruiquan Wang, Guohui Jin, Yanan Lu, Qingshan Li, Zhen Gao & Longjun Chen

Optimizing robot weaving width improves the microstructure and mechanical performance of 4043 aluminum alloy in CMT-WAAM

Shuangyao Liu[a], Yipu Sun[b] , Xi Yuan[c], Haozhong Lv[d], Ruiquan Wang[a], Guohui Jin[a], Yanan Lu[a], Qingshan Li[e], Zhen Gao[e], Longjun Chen[f,]

[a]Department of Additive Manufacturing, Zhejiang Polytechnic University of Mechanical & Electrical Engineering, Hangzhou, Zhejiang, 310053, China

[b]State Key Laboratory of Special Materials Surface Engineering, China Academy of Machinery Wuhan Research Institute of Material Protection Co., Ltd., Wuhan, 430030, China

[c]Research Institute of Natural Gas Technology, PetroChina Southwest Oil and Gas Field Company, Chengdu, 610213, China

[d]Science and Technology on Advanced Functional Composites Laboratory, Aerospace Research Institute of Materials & Processing Technology, Beijing, 100076, China

[e]Zhejiang Academy of Special Equipment Science, Hangzhou, Zhejiang, 310020, China

[f]Corrosion and Protection Center, Institute for Advanced Materials and Technology, University of Science and Technology Beijing, Beijing 100083, China

Abstract:

This study explores the influence of robot weaving width on the microstructure and mechanical properties of 4043 aluminum alloy thin-walled components fabricated using cold metal transfer (CMT)-based wire arc additive manufacturing (WAAM). Thin-wall structures composed of 20 layers were deposited using weaving widths of 4 mm, 6 mm, and 8 mm. As the weaving width increased, the microstructure evolved from coarse lath-like dendrites to finer dendrites. The phase composition remained consistent across all samples, consisting of Al and Si. Mechanical testing in both the travel (X) and building (Z) directions, along with hardness profiling through the wall height, revealed that a 6 mm weaving width achieved an optimal balance between structural refinement and mechanical performance. This condition also minimized anisotropy in mechanical performance. In contrast, at 8 mm, ductility decreased, and fracture surface at building (Z) direction exhibited mixed ductile-brittle fracture mode. These findings demonstrate that robot weaving width is a useful parameter in optimizing the WAAM-CMT process. A properly selected weaving width can enhance deposition efficiency without compromising material integrity, offering a practical approach for the rapid and reliable fabrication of large-scale aluminum alloy components.

Keywords: Wire and arc additive manufacturing; Cold metal transfer; Robot weaving width; 4043 Aluminum alloy; Mechanical property

Corresponding author: Yipu Sun, E-mail: sunyipu0309@163.com

Longjun Chen, E-mail: chenlongjun530@126.com

1. Introduction

Aluminum alloys are valued for their low density [1], excellent plasticity [2], high thermal conductivity [3], and strong corrosion resistance [4], making them essential materials in aerospace [5], automotive [6], and oil and gas industry [7,8]. As demand grows for lightweight and high-performance components with complex geometries, conventional manufacturing methods such as casting and forging often fall short due to limitations in flexibility, efficiency, and material utilization [9,10]. Additive manufacturing (AM) has emerged as a promising alternative, offering advantages such as reduced production costs, shorter lead times, high material efficiency, and the capability to fabricate intricate structures directly from digital models [11]. These benefits have led to widespread interest in applying AM techniques to aluminum alloy fabrication. However, not all AM methods are equally effective for aluminum alloys. Processes such as laser-based powder bed fusion face challenges due to the high reflectivity and thermal conductivity of aluminum, which can reduce laser energy absorption, impair part density, and limit the scalability of components [12,13].

Wire-arc additive manufacturing (WAAM) offers several advantages over other AM technologies, including high deposition efficiency, reduced material waste, relatively simple equipment requirements, and the capability to fabricate large components using conventional welding techniques [14]. WAAM has been shown to reduce component production time by 40-60 % and post-processing time by 15-20 %, making it a cost-effective and efficient solution for fabricating metal components [15]. Based on the type of heat source, WAAM can be categorized into four main processes: gas metal

arc welding (GMAW), gas tungsten arc welding (GTAW), plasma arcwelding (PAW), and cold metal transfer (CMT). While GMAW provides high deposition rates, its intense heat input often leads to instability in the molten pool, resulting in overflow, collapse, and poor dimensional accuracy [16]. GTAW and PAW processes, though capable of producing high-quality deposition, are highly sensitive to arc length variations and lack coaxial wire feeding [17]. This can introduce defects when the deposition direction changes, especially in thin-walled structures, thereby increasing anisotropy and limiting broader applicability.

In contrast, the CMT process offers precise control, low heat input, and virtually spatter-free deposition [18-20]. These features make it particularly well-suited for low-melting-point metals such as aluminum alloys [21-23]. By tailoring process parameters in CMT-based WAAM, it is possible to refine the microstructure and enhance the mechanical properties of aluminum components-an essential requirement for functional applications [24]. As a result, extensive research has been conducted on the influence of various CMT process parameters on aluminum alloy performance. For example, Feng et al. [25] reported improvements in microhardness through interlayer cooling, which mitigated the adverse effects of thermal accumulation. Chen et al. [26] demonstrated that increasing travel speed could enhance strength and ductility in aluminum alloys, surpassing properties typically seen in cast alloys. Additionally, incorporating CMT-pulsed has been shown to reduce porosity and improve wettability in the molten pool, leading to fewer gas inclusions and enhanced structural integrity [27]. Beyond performance optimization, fabrication efficiency remains a critical concern in CMT-based WAAM. Increasing aluminum alloys deposition within a limited timeframe is a priority, and introducing robotic weaving during deposition has emerged as a promising strategy to improve build efficiency [28]. However, the impact of robot weaving width on the resulting component geometry, microstructural characteristics and mechanical performance of aluminum alloys remains poorly understood.

In this study, 4043 aluminum alloy was selected as the research material because of its high forming efficiency, simple composition, ease of processing, and stable performance [29]. Using the WAAM-CMT process, thin-walled structures consisting of 20 layers were fabricated with three robot weaving widths-4 mm, 6 mm, and 8 mm-selected based on preliminary experimental results. The influence of weaving width on the microstructure and phase composition at various wall heights (bottom, middle, and top) was examined through metallographic analysis, scanning electron microscopy (SEM), energy dispersive spectroscopy (EDS), and X-ray diffraction (XRD). Grain orientation and grain size in the middle region were determined using electron back scatter diffraction (EBSD). Hardness distribution along the building direction (Z) was measured to evaluate vertical uniformity, while tensile tests were conducted in both the travel (X) and building (Z) directions to assess mechanical anisotropy. This work discusses how robot weaving width affects microstructural evolution and mechanical performance. By identifying optimal weaving width, the study aims to enhance deposition efficiency while maintaining desirable mechanical properties.

2. Experimental

2.1 Materials and equipment

4043 aluminum alloy (1.2 mm diameter) was used as filler wire and 6 mm thick AA6061 Al alloy plate (120 × 120 mm) served as substrate, with composition as shown in Table 1. Prior to deposition, the substrate surface was mechanically polished to remove oxide contamination. The deposition process employed a WAAM-CMT system, illustrated in Fig. 1. This setup comprised a KUKA KR60-3 robotic arm, a CMT welding torch, a wire feeder, a robotic controller, a programmable logic controller (PLC), a Fronius CMT TPS4000 power source, and an Ar shielding gas supply. To ensure precise control, a standardized coordinate system was established: The X-axis aligned with the robot's forward motion, the Z-axis corresponded to the vertical build direction of the thin-walled structure, and the Y-axis represented the lateral weaving direction during deposition.

2.2 Cold metal transfer process

The CMT process was controlled by six parameters: wire feed speed, pulse frequency, arc length correction, pulse correction, robot welding speed, and robot weaving width. Based on preliminary trials, these parameters were optimized to ensure stable deposition across 20 consecutive layers, as summarized in Table 2. To maintain consistent thermal conditions-critical for minimizing defects in additive manufacturing-interlayer temperature control and thermal input regulation were systematically implemented [30]. All samples were deposited under Ar gas protection. After depositing each layer, the robotic system automatically paused via an external signal control interface, allowing real-time monitoring of sample temperature using a contact thermocouple thermometer (equipped with K03B probe, PEAKMETER PM6501). Deposition resumed only when the substrate temperature dropped below 100 °C, ensuring uniform cooling and reducing residual stresses. As the build height increased, longer dwell times were required. To maintain stable heat input, as listed in Table 2 the wire feed speed and pulse frequency were gradually adjusted during the deposition process. Using this strategy, thin walled 4043 aluminum structures exceeding 100 mm in length and 65 mm in height were successfully fabricated. The final specimens exhibited widths of 13, 17, and 21 mm, corresponding to programmed weaving widths of 4, 6, and 8 mm, respectively (Fig. 2a–i). The robot's motion trajectory, designed using SprutCAM 14 software (SPRUT Technologies, Russia), followed a reciprocating path with a 1.2 mm interlayer overlap (travel direction (X)) and a 4 mm vertical step height between layers (Fig. 2j). Weaving widths of 4, 6, and 8 mm were tested to evaluate their influence on the alloy's microstructure and mechanical performance.

2.3 Microstructure characterization

Metallographic and phase analysis specimens were extracted from three regions of the 4043 aluminum alloy thin wall: the top zone (6 mm below the top surface), middle zone (40 mm above the substrate), and bottom zone (6 mm above the substrate). Specimen locations are indicated by yellow dashed

lines in Fig. 3(a), with sampling areas marked by blue dashed boxes in Fig. 3(d). Wire electrical discharge machining was used to ensure precise cutting with minimal thermal distortion. Following ASTM E3-11 and E407-07 standards, the specimens underwent mechanical polishing to achieve a mirror-like surface finish. The polished surfaces were then etched with Keller's reagent for 15 s to reveal microstructural features. After etching, samples were rinsed sequentially with deionized water and anhydrous ethanol to remove residues, followed by drying with cold air. Microstructural observations were conducted using a Leica DMI8C optical microscope (Leica Microsystems, Germany), and a FEI thermal field emission SEM. Elemental distribution was analyzed using an Oxford X-MAXN50 energy-dispersive spectrometer operated at an accelerating voltage of 15 kV. Statistical analysis of crystallographic information in the middle region of thin-walled 4043 aluminum alloy components was performed using EBSD (Zeiss EVO-18, Germany). The EBSD scans were conducted with a step size of 0.3 μm and an accelerating voltage of 30 kV. Data processing and analysis were carried out using Channel 5 software. Phase composition analysis was performed XRD (D8 Advance) with Cu-Kα radiation, at 40 kV and 40 mA, within a 2θ range of 20-90°.

2.4 Mechanical tests

Vickers microhardness testing was performed on the 4043 aluminum alloy thin walls using a FLC-50MV hardness tester (Japan) with a 1 kg load and 10 s dwell time. Measurements were taken along the building direction (Z-axis) centerline at 2 mm intervals (Fig. 3c). The relationship between weaving width and microhardness variations was analyzed by correlating hardness values with their vertical positions. Tensile properties were evaluated in the travel direction (X) and building direction (Z) orientations using an Instron universal testing machine with a contact extensometer. Specimens were extracted from locations marked in red dashed boxes (Fig. 3a). The specimen size was shown in Fig. 3(b). Testing began at a loading rate of 0.23 mm/min, increasing incrementally to 1 mm/min after surpassing 1% strain. Two replicates were

tested for each orientation to ensure statistical reliability. Fracture surfaces of the tensile specimens were examined using SEM (EVO-18, Germany) in secondary electron mode at 20 kV accelerating voltage to characterize failure.

3. Results

3.1 Appearance characteristics

The 4043 aluminum alloy thin-walled structures fabricated at weaving widths of 4, 6, and 8 mm exhibited distinct layered morphologies, as illustrated in Fig. 2(c, f, i). The layer height increased with wider robot weaving widths. In conventional WAAM-CMT processes, continuous single-direction deposition strategy often leads to structural expansion at the starting position and collapse at the endpoint of thin-walled builds [31,32]. However, collapse was observed at both the starting and ending positions of all samples in this study (Fig. 2(b, e, h)). This phenomenon is attributed to the interlayer temperature control strategy: Prolonged cooling intervals between layers reduced residual heat, but during subsequent deposition, the abrupt reheating of the cooler start/end regions caused excessive heat accumulation. This elevated melt pool temperatures, lowering liquid metal viscosity and surface tension, which destabilized the structure. In contrast, the central regions of the thin walls displayed stable layer formation. As the melt pool advanced along the travel direction (X), heat input and dissipation equilibrated, enabling consistent melt pool spreading and uniform layer thickness. This equilibrium minimized defects, resulting in a stable region with a high layer thickness.

3.2 Microstructure characterization

Figs. 4 and 5 present the microstructure of 4043 aluminum alloy thin walls fabricated at robot weaving widths of 4, 6, and 8 mm, as observed under optical and SEM, respectively. Corresponding elemental distributions obtained by EDS are also shown in Fig. 5. Microstructural features were analyzed at three height positions: top (Figs. 4(a-c), 5(a-c)), middle (Figs. 4(d-f), 5(d-f)), and bottom (Figs. 4(g-i), 5(g-i)). The implemented temperature control strategy maintained uniform microstructures across all regions, with minor influence from the weaving width. All samples exhibited a dendritic

structure consisting of lathy dendrites and interdendritic regions. In the 4 mm sample, the structure was dominated by plate-like dendrites. With increasing weaving width, a progressive transition toward spherical dendrites was observed: the 6 mm sample exhibited a mix of lathy and globular dendrites, with further increases in globular dendrites at 8 mm. EDS analyses revealed notable elemental segregation. Al was concentrated within the dendritic regions, whereas the interdendritic zones-displaying a rod-like distribution-were enriched in Si. Additionally, localized enrichment of Fe was observed in the interdendritic areas, coinciding with regions of O accumulation. This suggests the possible formation of iron oxides during the deposition process.

To quantitatively evaluate grain structure evolution and corroborate the SEM observations, EBSD analysis was conducted on the central region of thin-walled 4043 aluminum alloy specimens. Fig. 6 presents the inverse pole figure (IPF) maps and corresponding grain size distributions for samples fabricated with various robotic weaving widths. As shown in Fig. 6(a-c), the crystallographic orientations in the central region are largely random, indicating that variations in weaving width do not induce a pronounced preferred texture. The grain size results in Fig. 6(d-f) clearly demonstrate progressive grain refinement with increasing weaving width. As a weaving width of 4 mm, the microstructure is characterized by relatively coarse grains with a broad size distribution, with a substantial fraction exceeding 60 μm. When the weaving width is increased to 6 mm, the average grain size decreases to 36.58 μm (Fig. 6(e)). Further increasing the weaving width to 8 mm results in an average grain size of 32.05 μm (Fig. 6(f)), accompanied by a pronounced shift in the grain size distribution toward smaller sizes and an increase in grains smaller than 20 μm. This refinement is primarily attributed to the wider deposition width produced by larger weaving amplitudes, which increases the surface area exposed to the environment and enhances the cooling rate-conditions that promote the formation of finer dendrites (Fig. 2(a, d, g)) [24,33].

As shown in Fig. 7, XRD analysis of the 4043 aluminum alloy thin walls, fabricated at robot weaving widths of 4, 6, and 8 mm, revealed consistent phase compositions across the top, middle, and bottom regions. The phase composition was consistent across the top, middle, and bottom regions, with identical diffraction peak positions observed for all samples. This indicates that the weaving width did not affect the phase composition, which consisted of α-Al and Si. Both phases exhibit face-centered cubic (FCC) structures, corresponding to space groups Fm3m (225), and Fd3m (227), respectively [34]. Characteristic diffraction peaks of α-Al were observed at (111), (200), (220), (222), and (311) planes, while those of Si appeared on the (111), (220), and (311) planes. In all samples, the strongest peak was located on the (111) plane of α-Al, consistent with its close-packed structure and lower surface energy, which favors growth along this orientation [35]. However, in the middle and bottom regions of samples produced with 6 mm and 8 mm weaving widths, an increase in the intensity of the α-Al (220) peak was noted. This may be attributed to slower thermal diffusion in these regions, which suppresses growth along the (111) plane and promotes alternative crystallographic orientations [35].

3.3 Mechanical properties

Fig. 8 presents the microhardness distribution along the building direction (Z) in the longitudinal section of the 4043 aluminum alloy thin walls fabricated with robot weaving widths of 4, 6, and 8 mm. The average microhardness values for these samples were 40.4, 39.6, and 40.8 Hv, indicating that the overall weaving width had little impact on average hardness. However, the variation in weaving width influenced the microhardness gradient from the bottom to the top of the thin walls. Huang et al. [36] demonstrated that substrates act as heat sinks, accelerating cooling and promoting the formation of finer grains near the bottom of the wall. Similar observations were reported by Hong et al. [37] and Ashish et al. [38]. However, in contrast to these findings, the samples fabricated with 4 mm and 6 mm weaving widths exhibited a slight increase in hardness from bottom to top. This discrepancy is attributed to the

interlayer temperature control strategy during deposition, which extended cooling times. As a result, a more uniform and widely distributed Si phase formed, particularly in the middle and top regions (Fig. 5). The presence of this hard, brittle Si phase contributes to hardness enhancement by restricting dislocation movement [35].

Additionally, the increased wall thickness (Y direction) and corresponding differences in thermal gradients between the core and surface enhanced heat dissipation at the surface, promoting finer grain formation (Fig. 6). These thermal conditions favored the formation of finer grains compared to the 4 mm sample. According to the Hall-Petch relationship, which describes the inverse correlation between grain size and hardness [39], this grain refinement accounts for the more moderate increase in hardness observed in the middle and upper regions of the 6 mm sample relative to the 4 mm sample. When the weaving width was further increased to 8 mm, the microhardness displayed a slight downward trend from bottom to top. This reduction is likely associated with further grain refinement (Fig. 6), which, despite typically enhancing strength, may have resulted in a less favorable distribution of hard phases (Fig. 5), thereby lowering the overall hardness.

Fig. 9 presents the engineering stress-strain curves of 4043 aluminum alloy thin walls fabricated with robot weaving widths of 4, 6, and 8 mm, evaluated in both the travel direction (X, Fig. 9(a)) and the building direction (Z, Fig. 9(b)). Across all samples, the stress-strain behavior was broadly similar, featuring an initial elastic stage followed by a uniform plastic deformation stage. Then, a distinct non-uniform plastic deformation phase preceding fracture was observed in all cases, except for the sample with an 8 mm weaving width in the building direction (Z), where this stage was less pronounced. This deformation pattern is typical for WAAM-CMT aluminum alloys [40-42].The robot weaving width has a pronounced effect on mechanical properties, including ultimate tensile strength, yield strength, and elongation, as shown in Fig. 10. In the travel direction, the ultimate tensile strength (Fig. 10(a)) remains largely unchanged across various weaving widths. In contrast,

the ultimate tensile strength in the building direction is consistently lower than that in the travel direction. A slight increase is observed as the weaving width increases from 4 to 6 mm, while it drops clearly when the width reaches 8 mm.

Due to no distinct yield plateau was observed in any of the stress-strain curves, the $\sigma_{0.2}$ (as per GB/T 228.1-2010) was used to determine the yield strength, presented in Fig. 10(b). At a 4 mm weaving width, yield strengths in both directions are approximately 70 Mpa and show minimal difference. With a 6 mm width, yield strength decreases in both directions, more noticeably in the building direction. Samples produced with an 8 mm weaving width display the highest yield strength in the travel direction, while the building direction yield remains moderate. This leads to a pronounced anisotropy, with the largest directional difference in yield strength observed at this width. Fig. 10(c) shows the elongation varies with weaving width. Samples fabricated at 6 mm exhibit relatively high elongation in both directions, indicating balanced ductility. The 4 mm samples show good elongation in the travel direction but poor ductility in the building direction. In contrast, the 8 mm samples exhibit poor elongation in both directions, suggesting reduced plastic deformation capacity at this weaving width.

To further assess mechanical performance, as listed in Table 3, yield-to-tensile strength ratios were calculated for each condition. All samples show yield-to-tensile strength ratios below 0.6 in both directions, conforming good plasticity overall [43]. Notably, the 6 mm samples exhibit the lowest and same ratios in both directions. This suggests that a moderate increase in robot weaving width can enhance mechanical isotropy and reduce directional dependence of mechanical properties in WAAM-CMT processes.

Fig. 11 presents the fracture surface morphologies of 4043 aluminum alloy thin-wall samples fabricated with robot weaving widths of 4, 6, and 8 mm, examined in both the travel and building directions. In the travel direction (X), all samples exhibited numerous dimples on the fracture surfaces, indicative of ductile fracture behavior. The sample produced with a 6 mm weaving width (Fig. 11(b)) displayed finer and more uniformly distributed dimples,

suggesting improved ductility, consistent with the better elongation property. Conversely, the 8 mm sample (Fig. 10(c)) contained a greater number of larger, irregular pores, which contributed to its reduced mechanical performance. In the building direction, the fracture characteristics were more sensitive to changes in weaving width. At 4 mm and 6 mm widths, the fracture surfaces primarily showed ductile features. Compared to the 4 mm sample, the 6 mm sample exhibited more pronounced porosity, correlating with its diminished mechanical properties. At the largest weaving width of 8 mm (Fig. 11(f)), the fracture morphology shifted noticeably, displaying features of mixed ductile-brittle failure. In addition to a few dimples, inter-parallel tear ridges characteristic of quasi-cleavage fracture were observed. Additionally, pores were observed across all samples, though their size and distribution varied with weaving width. Further investigation is required to understand how pore size and distribution affect the mechanical properties of thin-walled 4043 aluminum alloy structures fabricated at various weaving widths.

4. Discussion

This study shows that a weaving width of 6 mm yields the most favorable combination of fracture resistance and deformation compatibility among the tested conditions. The observed mechanical improvements at 6 mm are closely linked to changes in microstructure induced by varying the weaving width. As the weaving width increases, so does the wall thickness along the Y-axis, which in turn enlarged the surface area of the deposited metal (Fig. 2). A larger surface area facilitates more efficient heat dissipation during deposition, promoting finer dendritic structures (Fig. 6) [25]. Finer dendrites can hinder crack propagation by increasing the extent of microstructural heterogeneity thereby enhancing tensile strength [32]. However, increasing the weaving width beyond an optimal range introduces adverse thermal effects. A greater surface area intensifies the temperature gradient between the wall's core and surface, leading to excessive undercooling [25,44]. This promotes the formation of globular dendrites (Fig. 4(f)), which are less effective at resisting crack propagation, resulting in reduced mechanical performance [45]. These thermal-

microstructural dynamics explain the improvement in mechanical properties from 4 to 6 mm weaving width (Table 3), and the subsequent decline when the width is increased to 8 mm (Fig. 10), which also altered the fracture pattern of the metal (Fig. 11).

Additionally, the implementation of a temperature control strategy during deposition, in combination with optimized weaving width, contributed to a more uniform microstructure throughout the height of the thin walls. This minimized the variation in mechanical properties along the building direction (Fig. 8), enhancing the structural consistency of the samples. This result is consistent with previous literature. For instance, Bansal et al.[46] demonstrated that reducing heat input while increasing scanning speed can decrease the number of defects in thin-walled aluminum alloy components fabricated via WAAM-CMT. Chen et al.[26] confirmed that the simultaneous adjustment of wire feed rate and travel speed effectively modifies heat input, which in turn modifies the microstructure morphology. Such control allows aluminum alloys fabricated by the WAAM-CMT process to achieve better mechanical properties than the cast counterparts. As mentioned above, the combined use of temperature control and a moderate robot weaving width enables microstructural refinement and thermal stabilization, thereby improving the mechanical integrity and production efficiency of WAAM-CMT fabricated 4043 aluminum alloy thin-walled components.

5. Conclusion

In this study, the effects of robot weaving width on microstructure and mechanical properties of WAAM-CMT 4043 aluminum alloys were investigated. The key findings are summarized as follows:

1. A robot weaving width of 6 mm yields the best balance of tensile strength, ductility, and isotropy in 4043 aluminum alloy thin walls. This width promotes finer dendritic structures due to enhanced heat dissipation, while avoiding excessive thermal gradients that degrade performance at 8 mm.

2. Wider weaving widths amplify surface-area cooling, resulting in finer dendritic structure. Excessive width introduces many globular dendrites and porosity, weakening crack resistance. The interlayer temperature control strategy ensures consistent dendritic refinement in the top, middle, and bottom.
3. Robot swing width changes the fracture pattern of 4043 aluminum alloy thin walls in the building direction. At weaving widths of 4 and 6 mm, samples exhibit ductile fracture characterized by dimples, while a swing width of 8 mm induces a mixed ductile-brittle fracture mode.
4. A moderate weaving width combined with active temperature control effectively reduces mechanical anisotropy and ensures structural uniformity along the building direction. This synergistic strategy stabilizes microstructure development throughout the deposition process, enhancing both mechanical consistency and manufacturing efficiency in WAAM-CMT-fabricated aluminum alloy components.

Data availability Statement

The data that support the findings of this study are available from the corresponding author upon reasonable request.

Authors Contributions

Shuanyao Liu: Data curation, Writing - original draft, Funding acquisition. **Yipu Sun:** Writing - review & editing. **Xi Yuan:** Validation. **Haozhong Lv:** Methodology. **Ruiquan Wang:** Investigation. **Cuohui Jin:** Formal analysis. **Yanan Lu:** Software. **Qingshan Li:** Resources. **Zhen Gao:** Software. **Longjun Chen:** Project administration, writing - review & editing.

Funding

The authors are grateful to General Scientific Research Project of Zhejiang Provincial Department of Education (Y202558220,

Y202456476), School-level Key Subjects of Zhejiang Polytechnic University of Mechanical & Electrical Engineering (A-0271-24-206), Visiting Engineer Research Program for Universities in Zhejiang Province (FG2024037).

Competing Interest

The authors declare that they have no known competing financial interests or personal relationships that could have appeared to influence the work reported in this paper.

Reference

1 Mondolfo, L. F. *Aluminum alloys: structure and properties*. (Elsevier, 2013).

2 Dai, R. *et al.* Achieving excellent strength and plasticity of aluminum alloy through refining and densifying precipitates. *Materials & Design* **248**, 113439 (2024). https://doi.org/https://doi.org/10.1016/j.matdes.2024.113439

3 Zhang, A. & Li, Y. Thermal Conductivity of Aluminum Alloys—A Review. **16**, 2972 (2023).

4 Liu, S., Li, Z., Gao, J. & Wang, W. Enhancing corrosion resistance of AZ31B magnesium alloy substrate in 3.5 % NaCl solution with Al-Si coating prepared by cold metal transfer-based wire arc additive manufacturing. *International Journal of Electrochemical Science* **19**, 100763 (2024). https://doi.org/https://doi.org/10.1016/j.ijoes.2024.100763

5 Starke, E. A. & Staley, J. T. Application of modern aluminum alloys to aircraft. *Progress in Aerospace Sciences* **32**, 131-172 (1996). https://doi.org/https://doi.org/10.1016/0376-0421(95)00004-6

6 Stojanovic, B., Bukvic, M. & Epler, I. Application of aluminum and aluminum alloys in engineering. *Applied Engineering Letters* **3**, 52-62 (2018).

7 Gelfgat, M. Y., Basovich, V. S. & Adelman, A. in *SPE Annual Technical Conference and Exhibition* SPE-97035-MS (2005).

8 Kolenchin, N. P., Kuskov, V. N. & Shadrina, P. N. New Technologies of Anodizing Components of Oil and Gas Industry Equipment Made of Aluminum Alloys. *Applied Mechanics and Materials* **770**, 121-125 (2015). https://doi.org/10.4028/www.scientific.net/AMM.770.121

9 Liu, J., Liu, Y., Hang, P. & Liu, Z. Development situation and market analysis of aluminum alloy modern extrusions. *Light Alloy Fabrication Technology* **41** (2013).

10 Dudek, P., Fajkiel, A. & Reguła, T. The research on the ablation casting technology for aluminium alloys. *Solid State Phenomena* **223**, 70-77 (2015).

11 Ford, S. & Despeisse, M. Additive manufacturing and sustainability: an exploratory study of the advantages and challenges. *Journal of Cleaner Production* **137**, 1573-1587 (2016). https://doi.org/https://doi.org/10.1016/j.jclepro.2016.04.150

12 Derekar, K. S. A review of wire arc additive manufacturing and advances in wire arc additive manufacturing of aluminium. *Materials Science and Technology* **34**, 895-916 (2018). https://doi.org/10.1080/02670836.2018.1455012

13 Miao, Q., Liu, M., Zhao, K., Ma, G. & Wu, D. Research progress on technologies of additive manufacturing of aluminum alloys. *Laser & Optoelectronics Progress* **55**, 011405 (2018).

14 Williams, S. W. *et al.* Wire + Arc Additive Manufacturing. *Materials Science and Technology* **32**, 641-647 (2016). https://doi.org/10.1179/1743284715Y.0000000073

15 Wu, B. *et al.* A review of the wire arc additive manufacturing of metals: properties, defects and quality improvement. *Journal of Manufacturing Processes* **35**, 127-139 (2018). https://doi.org/https://doi.org/10.1016/j.jmapro.2018.08.001

16 Ogino, Y., Asai, S. & Hirata, Y. Numerical simulation of WAAM process by a GMAW weld pool model. *Welding in the World* **62**, 393-401 (2018). https://doi.org/10.1007/s40194-018-0556-z

17 IvánTabernero, Paskual, A., Álvarez, P. & Suárez, A. Study on Arc Welding Processes for High Deposition Rate Additive Manufacturing. *Procedia CIRP* **68**, 358-362 (2018). https://doi.org/https://doi.org/10.1016/j.procir.2017.12.095

18 Fang, X. *et al.* Microstructure Evolution and Mechanical Behavior of 2219 Aluminum Alloys Additively Fabricated by the Cold Metal Transfer Process. *Materials* **11** (2018).

19 Gu, J. *et al.* Deformation microstructures and strengthening mechanisms for the wire+arc additively manufactured Al-Mg4.5Mn alloy with inter-layer rolling. *Materials Science and Engineering: A* **712**, 292-301 (2018). https://doi.org/https://doi.org/10.1016/j.msea.2017.11.113

20 Li, Y., Yun, Z., Zhang, W., Long, X. & Zhu, J. 3D Modelling of Layer-by-Layer Heat and Mass Transfer in Wire Arc Additive Manufacturing. *Additive Manufacturing Frontiers* **3**, 200159 (2024). https://doi.org/https://doi.org/10.1016/j.amf.2024.200159

21 Pan, Y., Yu, M., Xu, C., Zhang, J. & Geng, L. High-Performance 2319 Aluminum Alloy via CMT-WAAM: Microstructure, Porosity, and Mechanical Properties. *Metals* **14** (2024).

22 Kumar, S., Singh, G., Sharma, V. S. & Sekar, S. Investigation of process parameters for quality deposition of AL5356 using cold metal transfer wire arc additive manufacturing (CMT-WAAM). *The International Journal of Advanced Manufacturing Technology* **138**, 2313-2333 (2025). https://doi.org/10.1007/s00170-025-15524-9

23 Sarıkaya, M. *et al.* A review on aluminum alloys produced by wire arc additive manufacturing (WAAM): Applications, benefits, challenges and future trends. *Journal of Materials Research and Technology* **33**, 5643-5670 (2024). https://doi.org/https://doi.org/10.1016/j.jmrt.2024.10.212

24 Omiyale, B. O. *et al.* Cold metal transfer WAAM of aluminum alloys: influence of processing parameters. *The International Journal of Advanced Manufacturing Technology* **136**, 1967-1987 (2025). https://doi.org/10.1007/s00170-024-14989-4

25 Chen, F., Yang, Y. & Feng, H. Regional Control and Optimization of Heat Input during CMT by Wire Arc Additive Manufacturing: Modeling and Microstructure Effects. *Materials* **14** (2021).

26 Su, C., Chen, X., Gao, C. & Wang, Y. Effect of heat input on microstructure and mechanical properties of Al-Mg alloys fabricated by WAAM. *Applied Surface Science* **486**, 431-440 (2019). https://doi.org/https://doi.org/10.1016/j.apsusc.2019.04.255

27 Zhang, Z., Yan, J., Lu, X., Zhang, T. & Wang, H. Optimization of porosity and surface roughness of CMT-P wire arc additive manufacturing of AA2024 using response surface methodology and NSGA-Ⅱ. *Journal of Materials Research and Technology* **24**, 6923-6941 (2023). https://doi.org/https://doi.org/10.1016/j.jmrt.2023.04.259

28 Kim, C. K. *et al.* 3D weaving path optimization for enhanced surface quality in wire arc-based directed energy deposition. *Journal of Materials Processing Technology* **340**, 118838 (2025). https://doi.org/https://doi.org/10.1016/j.jmatprotec.2025.118838

29 Nie, Y. *et al.* Rapid prototyping of 4043 Al-alloy parts by cold metal transfer. *Science and Technology of Welding and Joining* **23**, 527-535 (2018). https://doi.org/10.1080/13621718.2018.1438236

30 Derekar, K. *et al.* Influence of Interpass Temperature on Wire Arc Additive Manufacturing (WAAM) of Aluminium Alloy Components. *MATEC Web of Conferences* **269**, 05001 (2019).

31 Liu, Y., Liu, Z., Zhou, G., He, C. & Zhang, J. Microstructures and Properties of Al-Mg Alloys Manufactured by WAAM-CMT. *Materials* **15** (2022).

32 Yang, X. *et al.* Microstructure and mechanical properties of wire and arc additive manufactured AZ31 magnesium alloy using cold metal transfer process. *Materials Science and Engineering: A* **774**, 138942 (2020). https://doi.org/https://doi.org/10.1016/j.msea.2020.138942

33 Yadav, L. K., Misra, J. P. & Tyagi, R. Microstructural, mechanical, and corrosion behaviour analysis of Monel 400 fabricated using CMT-WAAM.

Materials Today Communications **42**, 111153 (2025). https://doi.org/https://doi.org/10.1016/j.mtcomm.2024.111153

34 Kotlarski, G. *et al.* Structure Formation and Mechanical Properties of Wire Arc Additively Manufactured Al4043 (AlSi5) Components. *Metals* **14** (2024).

35 Miao, Q. *et al.* Comparative study of microstructure evaluation and mechanical properties of 4043 aluminum alloy fabricated by wire-based additive manufacturing. *Materials & Design* **186**, 108205 (2020). https://doi.org/https://doi.org/10.1016/j.matdes.2019.108205

36 Chang, T., Fang, X., Liu, G., Zhang, H. & Huang, K. Wire and arc additive manufacturing of dissimilar 2319 and 5B06 aluminum alloys. *Journal of Materials Science & Technology* **124**, 65-75 (2022). https://doi.org/https://doi.org/10.1016/j.jmst.2022.02.024

37 Yipeng, W. *et al.* Microstructure and mechanical properties of 7075/5356 aluminum alloy laminated composite fabricated by wire arc additive manufacturing. *Materials Letters* **367**, 136638 (2024). https://doi.org/https://doi.org/10.1016/j.matlet.2024.136638

38 Yadav, A., Srivastava, M., Jain, P. K. & Rathee, S. Microstructure transformations and improving wear resistance of austenitic stainless steel additively fabricated by arc-based DED process. *Defence Technology* **38**, 194-204 (2024). https://doi.org/https://doi.org/10.1016/j.dt.2024.02.006

39 Kesarwani, S. & Yuvaraj, N. Optimization of CMT-WAAM process parameters to minimize the porosity and surface roughness in bimetallic wall of aluminium alloys. *Welding in the World* **69**, 989-1002 (2025). https://doi.org/10.1007/s40194-024-01900-8

40 Hu, Z. *et al.* Microstructure and Mechanical Properties of a High-Ductility Al-Zn-Mg-Cu Aluminum Alloy Fabricated by Wire and Arc Additive Manufacturing. *Journal of Materials Engineering and Performance* **31**, 6459-6472 (2022). https://doi.org/10.1007/s11665-022-06715-6

41 Prasanna Nagasai, B., Malarvizhi, S. & Balasubramanian, V. Characterisation of Al–Mg Alloy Cylindrical Component Made by Wire Arc Additive Manufacturing Using Cold Metal Transfer Arc Welding Process. *Transactions of the Indian Institute of Metals* **75**, 2019-2030 (2022). https://doi.org/10.1007/s12666-022-02583-9

42 Wieczorowski, M., Pereira, A., Carou, D., Gapinski, B. & Ramírez, I. Characterization of 5356 Aluminum Walls Produced by Wire Arc Additive Manufacturing (WAAM). *Materials* **16** (2023).

43 Bannister, A. C., Ruiz Ocejo, J. & Gutierrez-Solana, F. Implications of the yield stress/tensile stress ratio to the SINTAP failure assessment diagrams for homogeneous materials. *Engineering Fracture Mechanics* **67**, 547-562 (2000). https://doi.org/https://doi.org/10.1016/S0013-7944(00)00073-4

44 Vazquez, L., Iturrioz, A., Lopez de Uralde, P. & Alvarez, P. Maximising the Deposition Rate of 5356 Aluminium Alloy by CMT-Twin-Based WAAM While Reducing Segregation-Related Problems by Local IR Thermography. *Metals* **13** (2023).

45 Blond, A., Firoozbakht, M., Bührig-Polaczek, A., Kaya, A. C. & Fleck, C. Relation Between Tensile Strut and Compressive Foam Deformation Behavior: Failure Mechanisms and the Influence of Dendritic Versus Globular Grain Structure in an AlSi7Mg0.3 (A356) Precision-Cast Open-Cell Foam. *Advanced Engineering Materials* **26**, 2400158 (2024). https://doi.org/https://doi.org/10.1002/adem.202400158

46 Singla, J., Kumar, N. & Bansal, A. Microstructural and mechanical properties of Al-5356 alloy structures fabricated using direct energy deposition (DED): In-pursuit to optimizing deposition parameters. *Materials Characterization* **216**, 114321 (2024). https://doi.org/https://doi.org/10.1016/j.matchar.2024.114321

Figures:

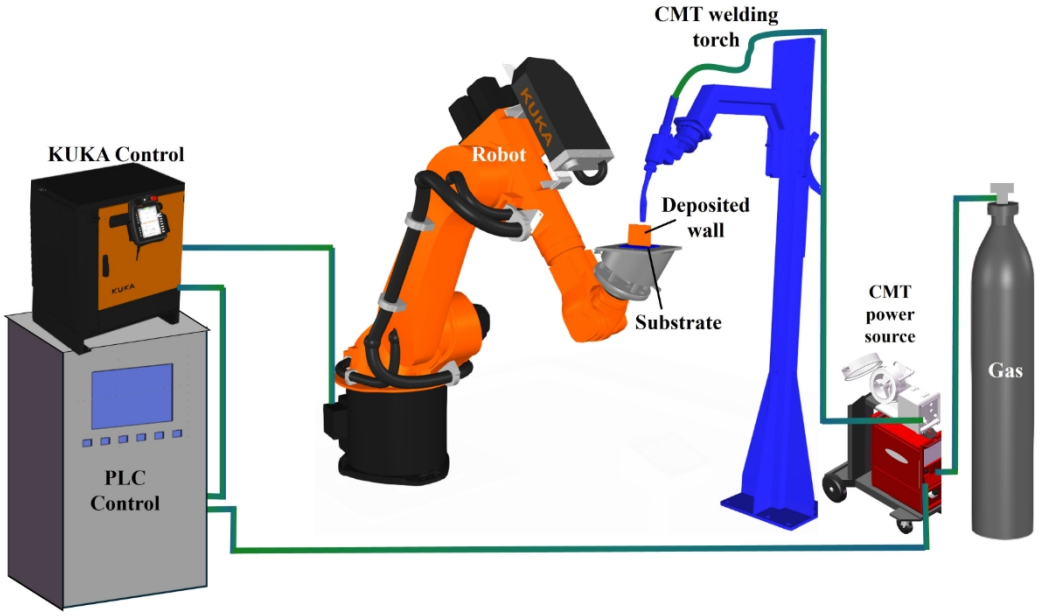

Fig. 1 Schematic diagram of the experimental setup used for CMT-WAAM

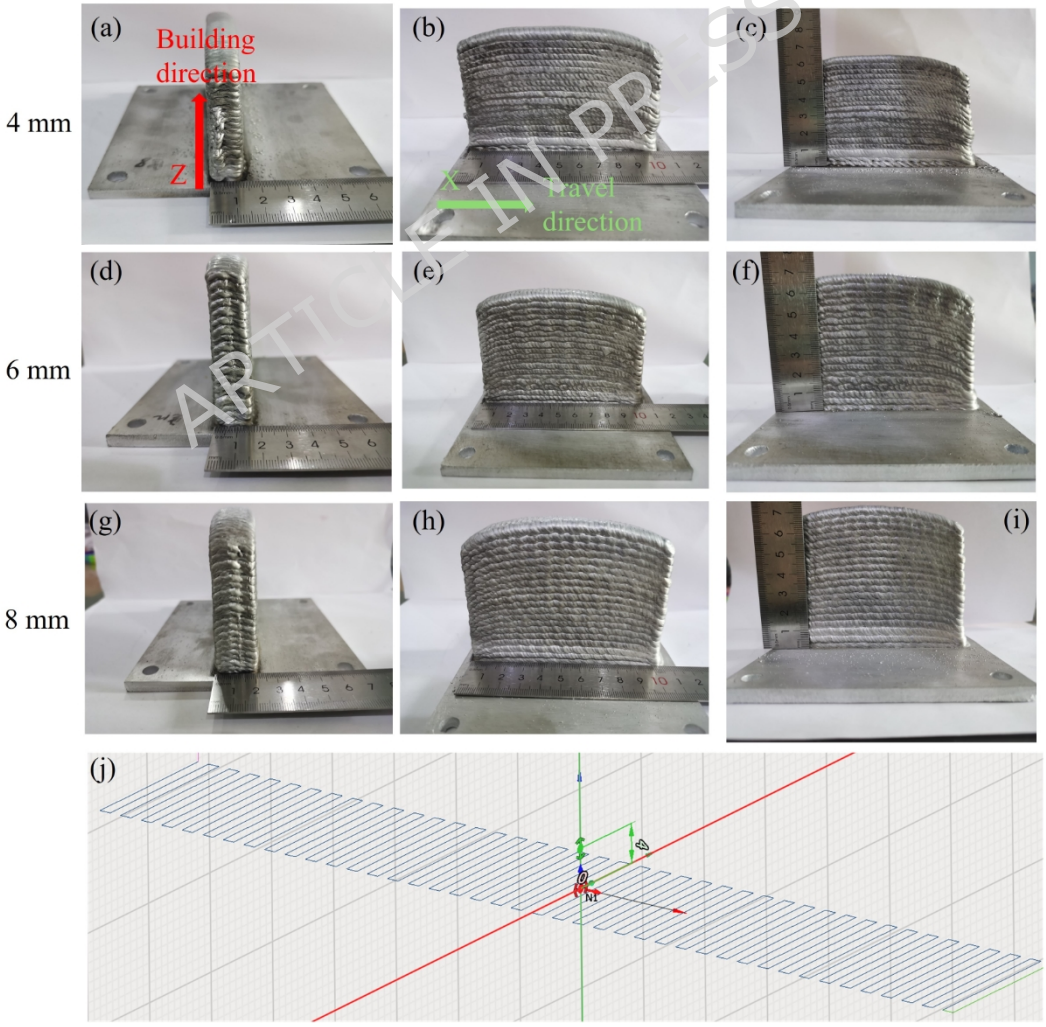

Fig. 2 External views of thin 4043 aluminum alloy walls deposited via the WAAM-CMT method with three robot weaving widths. **(a-c)** show the width, length, and height for a 4 mm weaving; **(d-f)** for a 6 mm weaving; and **(g-i)** for an 8 mm swing. **(j)** is a schematic of the robot weaving path.

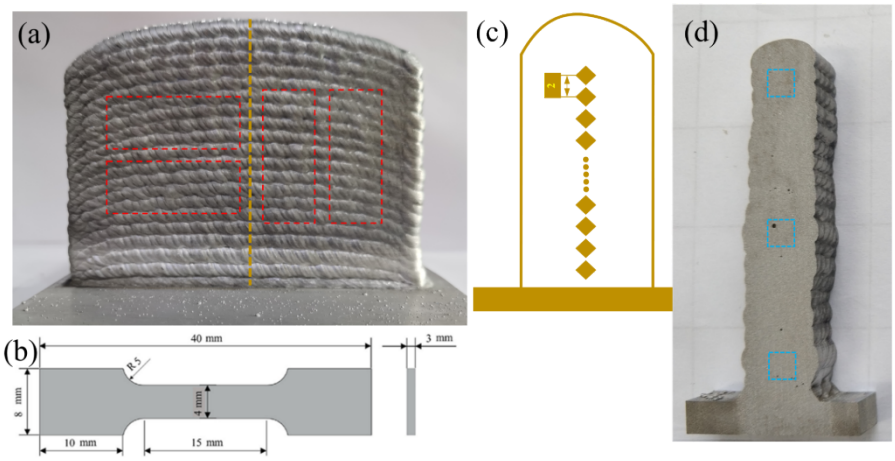

Fig. 3 The schematic illustrates that in **(a)** the red dashed box marks the tensile sample's location and orientation, while the tan dashed line indicates that hardness and metallographic test site. **(b)** shows the tensile sample dimensions (in mm), **(c)** shows the microhardness test location, and **(d)** shows the top, middle, and bottom metallographic sampling sites.

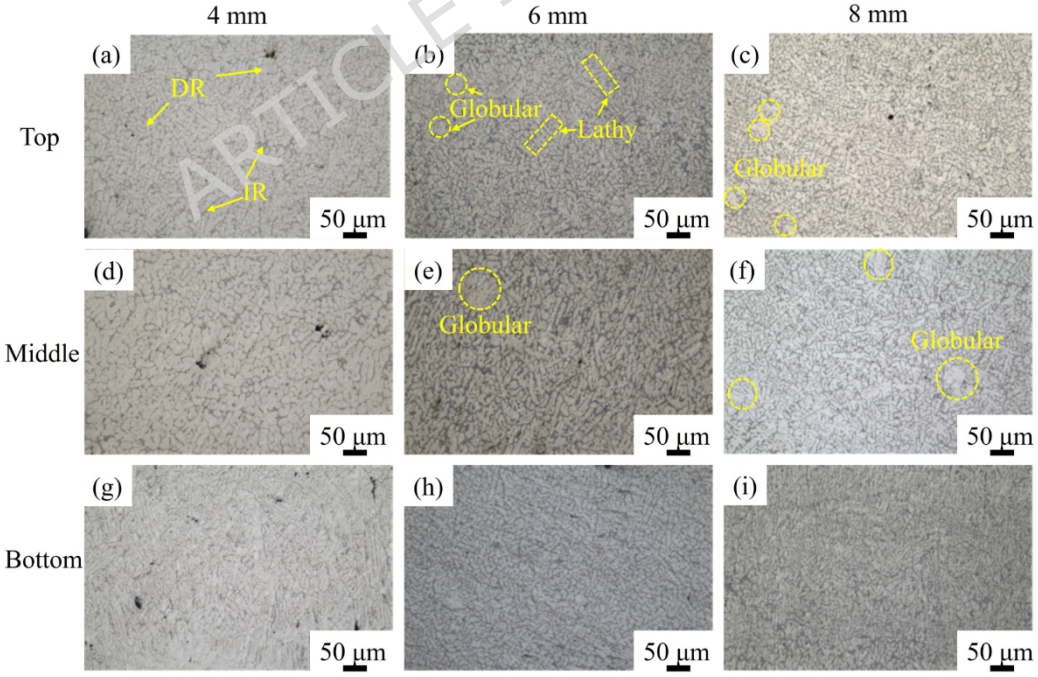

Fig. 4 Optical micrographs of the top **(a–c)**, middle **(d–f)**, and bottom **(g–i)** regions of 4043 aluminum alloy thin walls at three robotic weaving widths: 4 mm **(a, d, g)**, 6 mm **(b, e, h)**, and 8 mm **(c, f, i)**. DR: dendrite, IR: interdendrite.

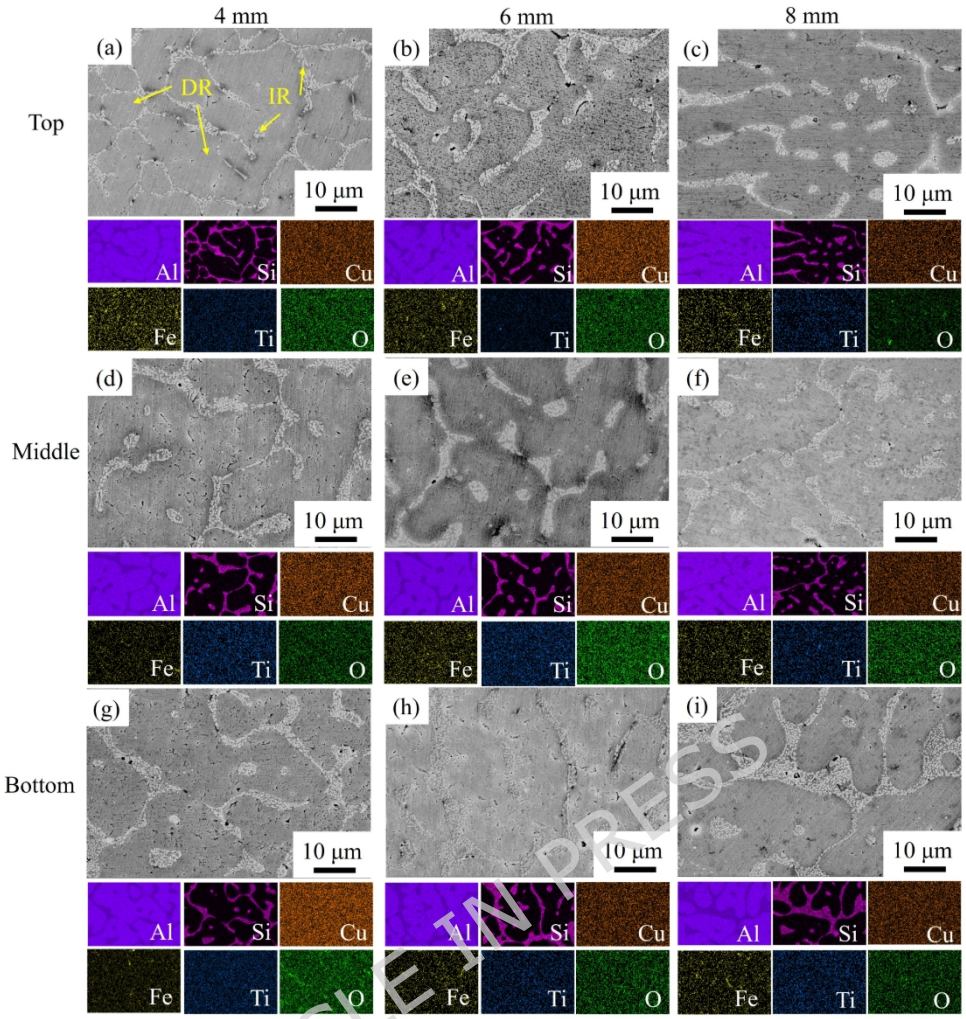

Fig. 5 The SEM images and the element distribution of the top **(a–c)**, middle **(d–f)**, and bottom **(g-i)** regions of 4043 aluminum alloy thin walls at three robotic weaving widths: 4 mm **(a, d, g)**, 6 mm **(b, e, h)**, and 8 mm **(c, f, i)**.

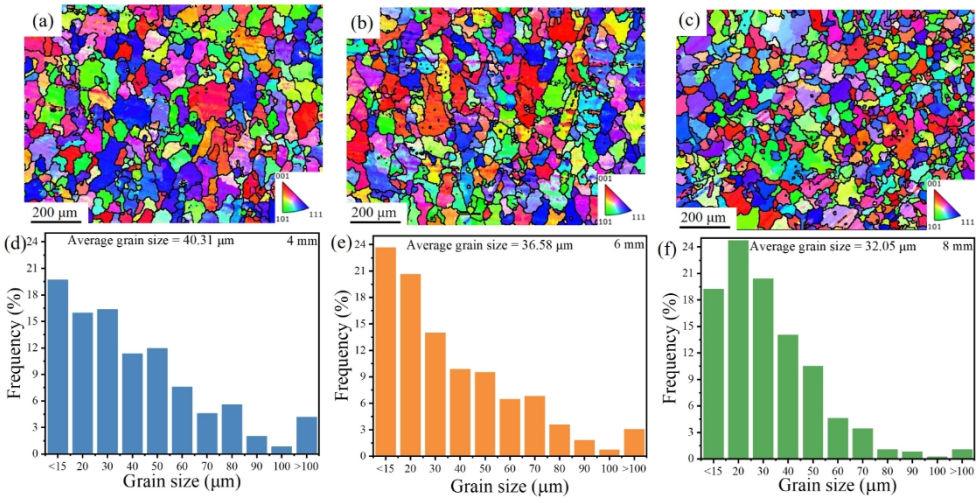

Fig. 6 EBSD images from the middle region of 4043 aluminum alloy thin walls fabricated at (a, d) 4 mm, (b, e) 6 mm, and (c, f) 8 mm robotic weaving

widths: (a-c) inverse pole figure, (d-f) grain size distributions with average grain sizes.

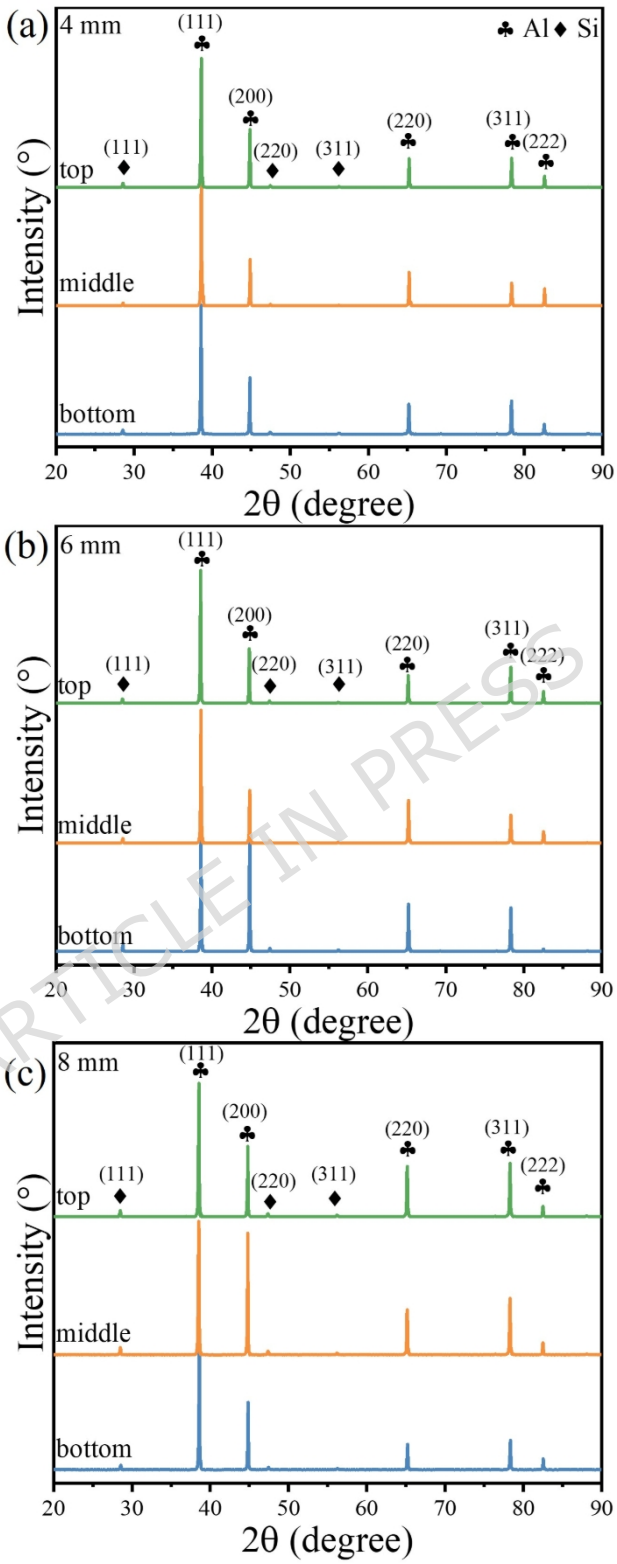

Fig. 7 XRD results from the Y-Z cross-sections (perpendicular to the X travel direction) of the top, middle, and bottom regions of 4043 aluminum alloy thin walls formed at three robot weaving widths: **(a)** 4 mm, **(b)** 6mm, and **(c)** 8 mm.

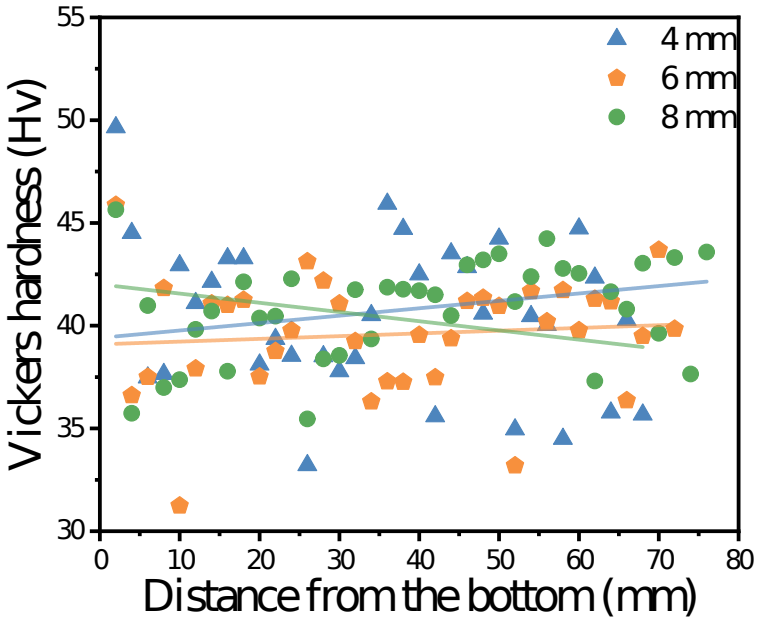

Fig. 8 Microhardness measurements along the build direction (Z) of 4043 aluminum alloy thin walls fabricated with robot weaving widths of 4 mm, 6 mm, and 8 mm.

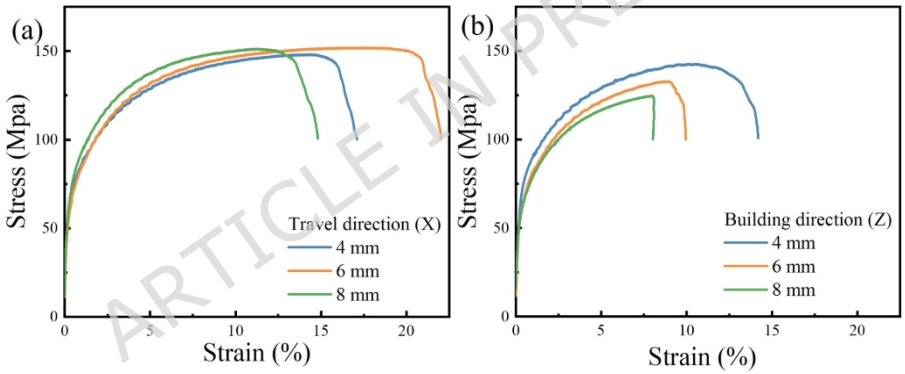

Fig. 9 Stress-strain graph of 4043 aluminum alloy thin walls fabricated with robot weaving widths of 4 mm, 6 mm, and 8 mm **(a)** travel direction, **(b)** building direction.

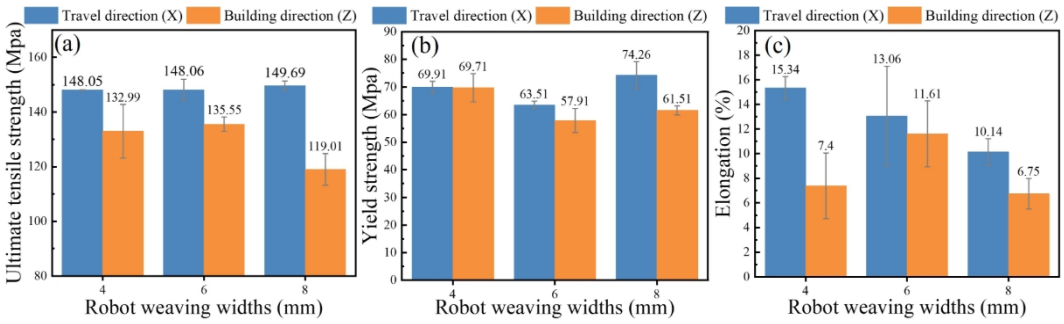

Fig. 10 The **(a)** ultimate tensile strength, **(b)** yield strength, and **(c)** elongation testing results of 4043 aluminum alloy thin walls fabricated with robot weaving widths of 4 mm, 6 mm, and 8 mm.

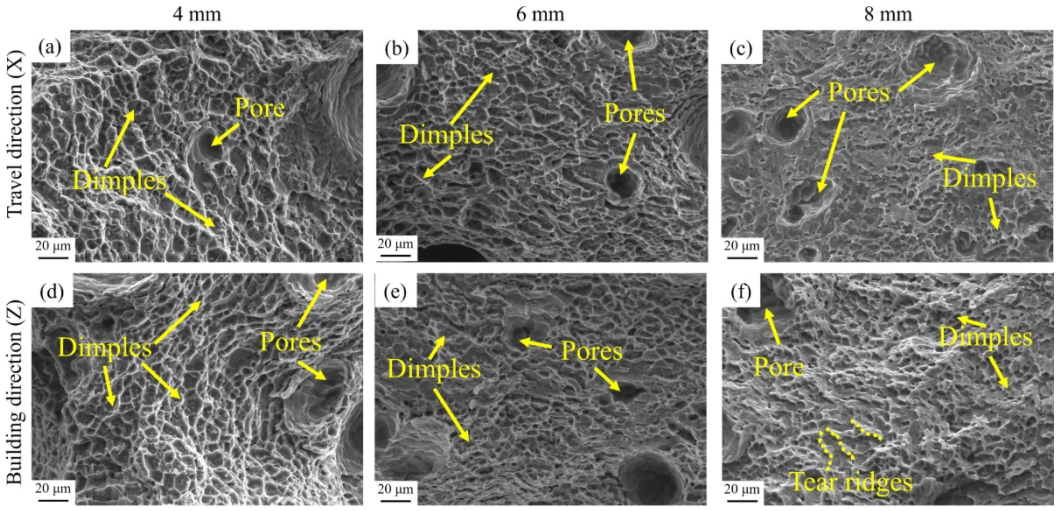

Fig. 11 SEM micrographs of the fracture morphologies of 4043 aluminum alloy thin walls fabricated with robot weaving widths of 4 mm **(a, d)**, 6 mm **(b, e)**, and 8 mm **(c, f)** in **(a-c)** the travel direction (X), **(d-f)** the building direction (Z).

Tables:

Table 1 Chemical compositions (wt.%) of the 4043 Al alloy filler wire and AA6061 Al alloy plate.

	Mg	Si	Fe	Cu	Mn	Zn	Ti	Al
ER4043	≤ 0.05	5.00	≤ 0.80	≤ 0.30	≤ 0.05	≤ 0.10	≤ 0.20	Bal.
AA6061	1.009	0.617	0.471	0.231	0.098	≤ 0.50	≤ 0.20	Bal.

Table 2 Layer-by-layer WAAM-CMT settings for thin-walled 4043 aluminum alloy deposition.

Layers		Wire feed speed (m/min)	Pulse frequency (Hz)	Arc length correction (%)	Robot welding speed (mm/s)	Pulse correction	Robot weaving width (mm)
1	Cold Metal Transfer + Pulse	4.0	3	10	11	-0.5	4/6/8
2		3.6	2.5	10			
3		3.6	2.5	5			
4		3.5	3	0			
5		3.4	3	5			
6		3.4	3	0			
7		3.3	3	0			
8		3.2	3	0			
9		3.2	3	0			
10		3.2	3	0			
11		3.2	3	0			
12		3.2	3	0			
13		3.1	3	0			
14		3.1	3	0			
15		3.1	3	0			
16		3.0	3	0			
17		3.0	3	0			
18		3.0	3	0			
19		3.0	3	0			
20		3.0	3	0			

Table 3 Yield-to-tensile strength ratios of 4043 aluminum alloy thin walls fabricated at three robot weaving widths (4 mm, 6 mm, and 8 mm) in the travel (X) and building (Z) directions.

Weaving width	Yield-to-tensile strength ratios	
	Travel direction (X)	Building direction (Z)
4 mm	0.47	0.52
6 mm	0.43	0.43
8 mm	0.50	0.52